# Journal of Materials Chemistry A



# **PAPER**

View Article Online
View Journal | View Issue



Cite this: J. Mater. Chem. A, 2025, 13, 31065

# One nanometer matters: quantum-induced discontinuity in the oxygen reduction reaction catalyzed by platinum nanoparticles

Zhuoya Deng, a Yuanyuan Liu, a Pengfei Wang, Zhunda Zhu, a Nutthira Pakkang, Garbis Atam Akceoglu, Sangwoo Chae, a Yasuyuki Sawada, Abc Li Yang and Nagahiro Saito a Nagahiro Saito

Quantum-induced discontinuity in the oxygen reduction reaction (ORR) catalyzed by Pt nanoparticles (NPs) occurs at the  $\sim$ 1.0 nm scale. Using a controlled solution plasma method, we synthesized monodisperse, surfactant-free  $\sim$ 1.0-nm Pt NPs uniformly supported on single-walled carbon nanotubes. Electrochemical evaluation revealed a pronounced deviation from the classical size-scaling behavior: the catalytic activity decreased with decreasing Pt NP diameter from 2.5 to 1.5 nm but unexpectedly increased at ~1.0 nm. High-resolution structural and spectroscopic analyses confirmed a critical transition around 1.5 nm, which separates the classical metallic behavior from a regime governed by quantum confinement. Despite their partial structural disorder, these quantum-sized clusters exhibited superior ORR performance, attributed to discrete electronic states, altered d-band structures and a high density of low-coordination active sites. The catalysts also demonstrated high durability, retaining ~90% of their reduction current after 2000 cycles with <5% particle growth in acidic media. In particular, the superior ORR performance at  $\sim$ 1.0 nm is consistent with the formation of magic number clusters exhibiting high symmetry, closed shell stability, and facet-specific reactivity. These structures deviate from conventional crystal habits, favoring icosahedral or truncated geometries rich in undercoordinated edge and corner atoms. The resulting disruption of long-range order and emergence of localized quantum states redefine the catalytic paradigm at this scale. This abrupt improvement in ORR performance establishes a fundamental boundary between classical and quantum electrocatalysis. By reframing ultrasmall Pt NPs as quantum objects rather than miniature metals, this study introduces a new design principle: harnessing quantum effects and symmetry-driven structural motifs for the rational design of next-generation catalysts in sustainable energy technologies.

Received 18th June 2025 Accepted 3rd August 2025

DOI: 10.1039/d5ta04934b

rsc.li/materials-a

#### Introduction

The development of advanced electrocatalysts for the oxygen reduction reaction (ORR) is a critical challenge in the quest for efficient and cost-effective fuel cells.<sup>1-4</sup> Pt remains the most widely used ORR catalyst and represents the state-of-the-art

material for significantly enhancing the sluggish kinetics of the ORR.5 However, owing to its scarcity and cost, further optimization of its catalytic performance is required, especially at the nanoscale, where the structure-activity relationships become extremely complex.<sup>6-9</sup> Over the past two decades, the size-dependent ORR activity of Pt nanoparticles (NPs) has attracted considerable attention.10 Garlyyev et al.11 demonstrated that Pt NPs exhibit a peak mass activity (MA) at a size of around 1.1 nm, which is attributed to the high density of surface atoms with intermediate generalized coordination numbers (GCNs) between 7.5 and 8.3, typically found on (111) terraces and their edges. Rück et al.12 proposed a Boltzmanntype model based on GCNs, emphasizing that the distribution of intermediate-coordinated sites determines the catalytic activity and varies with the particle size and morphology. Moreover, Imaoka et al. showed that even atomically defined Pt<sub>13</sub>-Pt<sub>19</sub> clusters exhibit a nonmonotonic size-activity relationship, with Pt<sub>19</sub> showing a distinct maximum in ORR performance due to its edge-rich geometry and orbital

<sup>&</sup>lt;sup>a</sup>Department of Chemical Systems Engineering, Graduate School of Engineering, Nagoya University, Furo-cho, Chikusa-ku, Nagoya 464-8603, Japan. E-mail: saito.nagahiro.z7@f.mail.nagoya-u.ac.jp

<sup>&</sup>lt;sup>b</sup>Department of International Collaborative Program in Sustainable Materials and Technology for Industries between Nagoya University and Chulalongkorn University, Graduate School of Engineering, Nagoya University, Furo-cho, Chikusa-ku, Nagoya 464-8603, Japan

Institute of Innovation for Future Society, Nagoya University, Furo-cho, Chikusa-ku, Nagoya 464-8603, Japan

d'School of Chemistry and Chemical Engineering, Frontiers Science Center for transformative Molecules, Shanghai Jiao Tong University, Shanghai 200240, China Conjoint Research Laboratory in Nagoya University, Shinshu University, Furo-cho, Chikusa-ku, Nagoya 464-8603, Japan

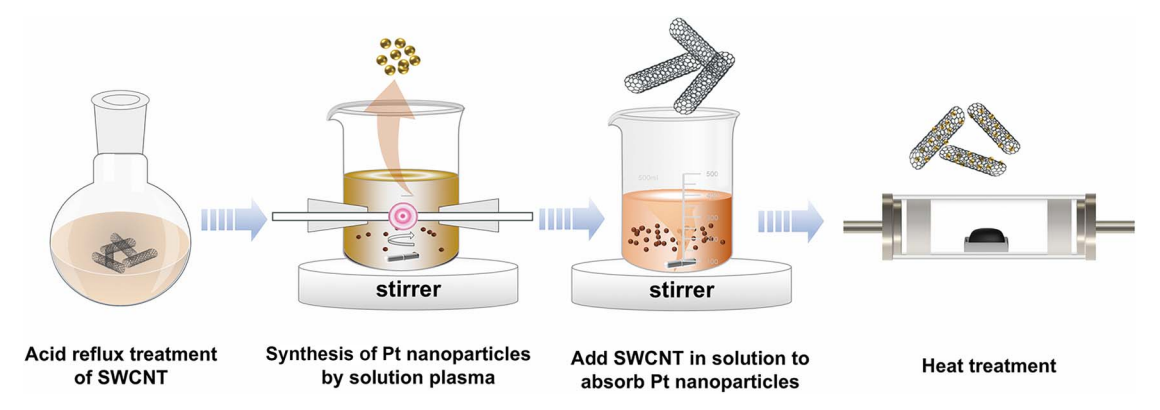


Fig. 1 Schematic of the solution plasma synthesis method for the preparation of monodisperse Pt nanoparticles supported on SWCNTs.

localization.<sup>12</sup> These results are supported by theory. For instance, Tripković *et al.*<sup>13</sup> predicted a maximum in MA near 3 nm using density functional theory (DFT) calculations. Yano *et al.*<sup>14</sup> used <sup>195</sup>Pt NMR spectroscopy to show that a significant electronic restructuring occurs below  $\sim$ 2 nm. Tritsaris *et al.*<sup>15</sup> also emphasized the key role of the active site distribution in the 2–4 nm range.

However, it remains unresolved whether the ORR activity continues into the subnanometer scale or breaks down owing to emerging quantum effects. Interestingly, Shao  $et\ al.^{16}$  observed a sharp decrease in activity as Pt NPs shrank from 2.2 to 1.3 nm, which they attributed to excessive oxygen binding at low-GCN sites. Such behavior is consistent with DFT predictions showing that undercoordinated atoms overstabilize adsorbates, thereby reducing the turnover frequency. Notably, Porch  $et\ al.$  demonstrated that even for precisely deposited  $et Pt_n$  clusters ( $et Pt_n$ ), the ORR activity correlates strongly with Pt 4f binding energy, indicating the dominant role of quantum-level electronic structures at the subnanometer scale. Additional complicating factors include strain, ligand effects, and interparticle interactions, although most studies have focused on the classical metallic NP regime.

To investigate whether classical size-activity relationships remain valid at smaller scales, we synthesized monodisperse  $\sim$ 1.0-nm Pt NPs supported on single-walled carbon nanotubes (SWCNTs) using a controlled solution plasma method. A preliminary electrochemical evaluation revealed a nonmonotonic trend: although the MA decreased with decreasing NP size from 2.5 to 1.5 nm, it seemed to recover at  $\sim$ 1.0 nm. This unexpected behavior suggests the existence of a critical threshold around 1.5 nm, below which quantum effects can override the classical behavior. Guided by this observation, we hypothesized that Pt NPs at the 1.0 nm scale undergo a transition from classical to quantum catalytic behavior, characterized by discrete electronic states, charge localization, and structural disorder. Such a transition would be analogous to Mott-type metal-insulator transitions,20 where reduced dimensionality and carrier delocalization lead to quantum-induced phase changes. Wang et al.21 showed that Pt clusters below 1.5 nm exhibit amorphous geometries and discrete energy levels, and Wang et al.22 demonstrated that ligand-stabilized Pt30 clusters

show high ORR activity. Meanwhile, Li *et al.*<sup>23</sup> used DFT calculations to show that Pt<sub>3</sub> clusters on Co@Pd substrates exhibit spin-polarized states with enhanced reactivity.

Nevertheless, single-atom catalysts and ligand-protected subnanoclusters suffer from stability and integration limitations.<sup>24–27</sup> In contrast, naked 1.0 nm Pt NPs offer the possibility of constructing ligand-free, structurally robust, and electronically quantum-confined systems. Unfortunately, their synthesis is challenging owing to aggregation and monodispersity issues.

In this work, we overcome these limitations using a solution plasma method that allows the uniform and stabilizer-free deposition of 1.0-nm Pt NPs on SWCNTs followed by heat treatment (HT) (Fig. 1, Tables S1 and S2). This approach provides direct access to the quantum-confined catalytic regime and allows us to systematically investigate whether these particles represent a different class of electrocatalysts. Recent studies further suggest that classical d-band theory may no longer predict ORR trends for Pt<sub>3-9</sub> clusters, implying that conventional scaling relations break down at the quantum cluster scale.28 To interpret the observed discontinuity, we also consider insights from surface science. Clavilier et al.29 and Hoshi<sup>30,31</sup> showed that the local terrace width and interfacial modification profoundly influence the ORR kinetics on Pt 111, which suggests that subtle structural and electronic rearrangements at the nanoscale may have an outsized effect on the reactivity.

Overall, this study investigates whether ultrasmall Pt NPs should be considered not as miniature metal particles but as quantum-defined catalytic entities governed by nonclassical structure–activity relationships, aiming to define the threshold between classical and quantum electrocatalysis. As a result, we propose a novel strategy based on the use of quantum effects as a design principle for next-generation ORR catalysts.

### 2. Results and discussion

TEM analysis (Fig. 2 and Table S3) revealed changes in the particle size of the Pt NPs during HT at 300600 °C. The samples were labelled according to the HT temperature as follows: Pt/SWCNT is the sample obtained immediately after synthesis

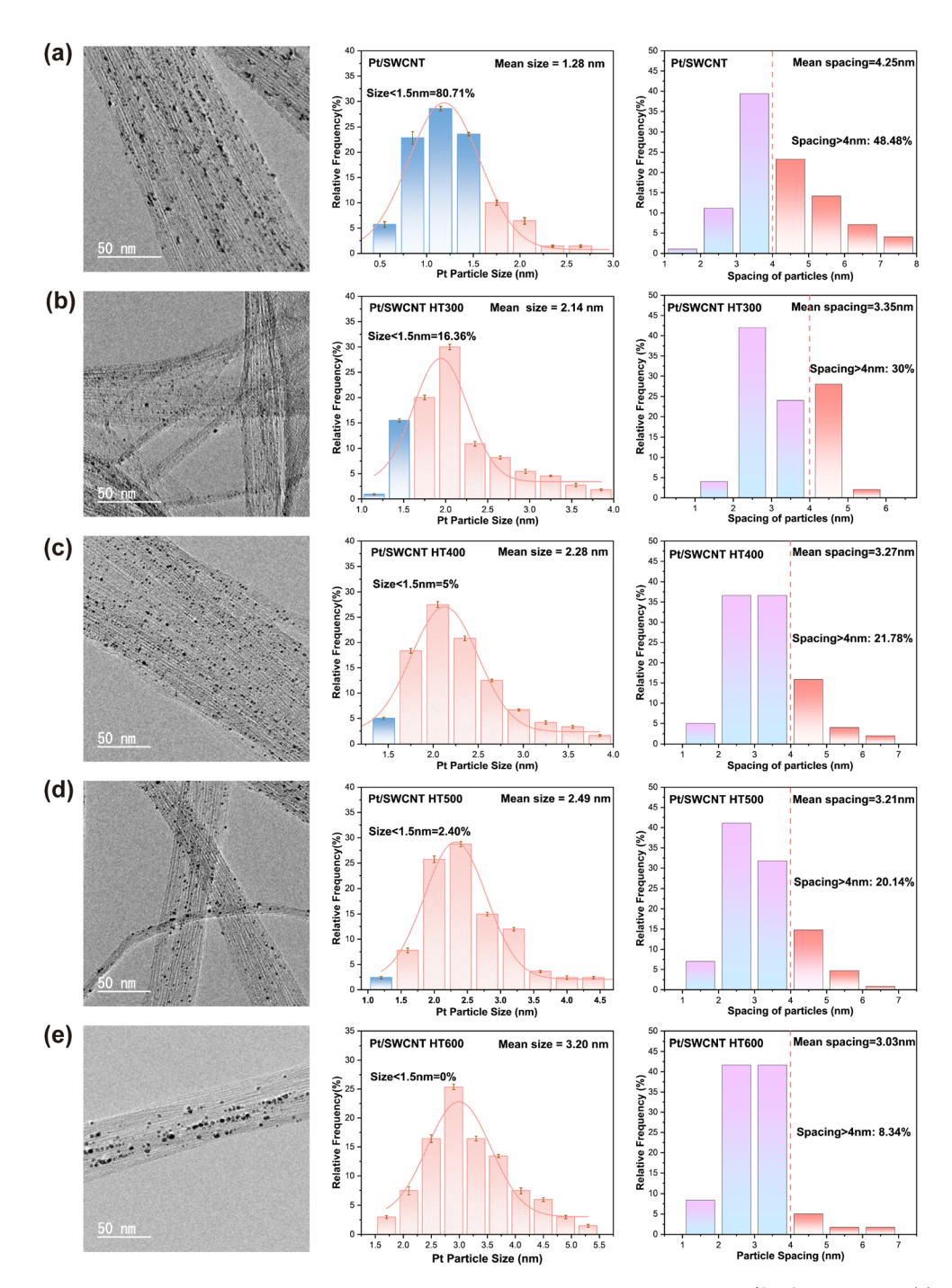


Fig. 2 High-resolution TEM images and the corresponding particle size distribution histograms of the Pt/SWCNT catalysts: (a) as-synthesized Pt/SWCNT (~1.28 nm), (b) Pt/SWCNT HT300, (c) Pt/SWCNT HT400, (d) Pt/SWCNT HT500, and (e) Pt/SWCNT HT600.

and Pt/SWCNT HT300, Pt/SWCNT HT400, Pt/SWCNT HT500, and Pt/SWCNT HT600 are the samples subjected to HT at 300  $^{\circ}$  C, 400  $^{\circ}$ C, 500  $^{\circ}$ C, and 600  $^{\circ}$ C, respectively. In Pt/SWCNT, the average diameter of the Pt NPs was  $\sim$ 1.28 nm and the average interparticle distance was  $\sim$ 4.25 nm. Approximately, 80.71% of the measured Pt NPs were smaller than 1.5 nm in diameter. With the stepwise HT, the average particle diameter increased from 2.14 nm for Pt/SWCNT HT300 to 3.20 nm for Pt/SWCNT HT600 and the interparticle distance decreased to  $\sim$ 3.03 nm,

confirming the occurrence of particle growth and partial agglomeration. Most importantly, the ratio of NPs with diameters smaller than 1.5 nm decreased sharply from 80.71% for Pt/SWCNT to 16.36% for Pt/SWCNT HT300, indicating a clear transition out of the quantum-confined regime.

Fig. 3a shows the powder X-ray diffraction (XRD) patterns of the Pt/SWCNT samples before and after HT in a  $H_2$ -Ar gas mixture. The diffraction peaks observed at approximately 39.7°, 46.2°, 67.5°, 81.3°, and 85.7° correspond to the 111, 200, 220,

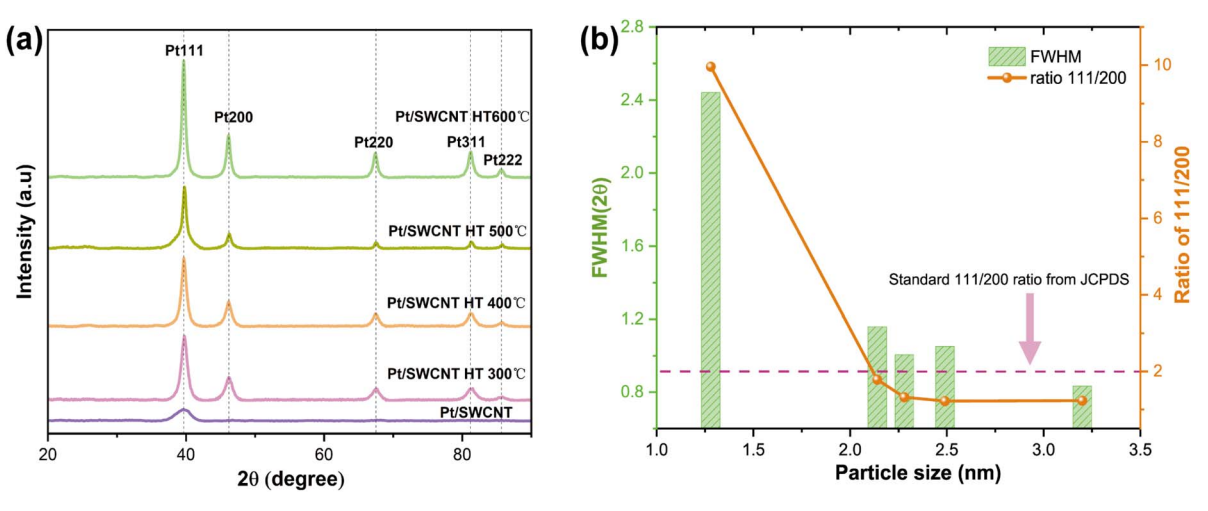


Fig. 3 (a) X-ray diffraction patterns of the Pt/SWCNT catalysts subjected to different heat treatment temperatures. (b) Enlarged view of the Pt 111 diffraction peak, demonstrating size-dependent crystallinity.

311, and 222 reflections of face-centered cubic Pt (JCPDS No. 04-0802). However, in the case of Pt/SWCNT without heat treatment, the intensity of the 111 reflection was the lowest and the 200 reflection was almost non-existent. Such XRD patterns are characteristic of NPs with a size of around 1 nm because structural disorder occurs when the diameter of the NPs approaches this scale. As shown in Fig. 3b, the full width at half maximum (FWHM) of the 111 reflection decreased steadily from 2.48° to 0.86° with increasing heat treatment temperature, which is consistent with an improvement in crystallinity. The intensity ratio of the 111 and 200 reflections  $(I_{111}/I_{200})$ , is quantitatively analysed and is plotted in Fig. 3b along with the standard intensity ratio from JCPDS for comparison. It is noteworthy that the  $I_{111}/I_{200}$  of the untreated Pt/SWCNT (9.6) deviates significantly from the value for bulk Pt ( $\sim$ 2). This difference is due to size-dependent anisotropic growth, which becomes pronounced when the critical dimension reaches about 1 nm. At this nanoscale, Pt NPs tend to expose the 111 plane rather than forming a perfect spherical structure, resulting in a truncated octahedral structure. In other words, as shown in Fig. 3b, the main crystal shape on the surface is the 111 plane. Moreover, the increase in the intensity of the XRD pattern reflections suggests that HT greatly improved the crystallinity of the Pt NPs. These results indicate the presence of Pt NPs smaller than 1 nm during the synthesis process. Typically, large Pt particles that are not affected by nanoscale effects have a nearly spherical morphology and a reflectance intensity ratio of about 2. However, owing to the quantum size effect, the relative area of the 111 plane increases and the particle morphology deviates from a sphere.21,32-34

Fig. 4a and b shows the Pt 4f and C 1s X-ray photoelectron spectroscopy (XPS) spectra of the Pt/SWCNT samples, respectively, before and after HT, together with the reference spectrum of commercially available 20 wt% Pt/C. Fig. 4c shows the relative proportions of the Pt<sup>4+</sup>, Pt<sup>2+</sup>, and Pt<sup>0</sup> chemical states. Fig. 4d shows the Pt<sup>2+</sup>/Pt<sup>0</sup> ratio and the FWHM of the C–C peak. The Pt 4f peaks were fitted with Gaussian–Lorentzian mixed functions,

and the binding energies were referenced to metallic Pt (Pt<sup>0</sup>, 71.2 eV for Pt  $4f_{7/2}$ ), Pt<sup>2+</sup> (72.5 eV), and Pt<sup>4+</sup> (74.0 eV).<sup>35</sup> The fitting results showed that the Pt surface generated by the solution plasma contained a relatively high proportion of oxidized states (Pt<sup>2+</sup> and Pt<sup>4+</sup>). With increasing HT temperature, the proportion of Pt<sup>0</sup> increased from 37% for Pt/SWCNT to 46% for Pt/SWCNT HT600, which indicates that the Pt NPs were gradually reduced by HT. However, no direct correlation between the oxidation state distribution and the ORR activity was observed. For example, although Pt/SWCNT HT600 had the highest Pt<sup>0</sup> content, its MA (242.6 mA mg<sup>-1</sup>) was much lower than that of quantum-sized Pt/SWCNT (552.9 mA mg<sup>-1</sup>). This indicates that the catalytic performance is mainly determined by the structural and electronic configuration rather than the oxidation state alone. The deconvoluted C 1s spectra of Pt/ SWCNT and its thermally treated counterparts exhibit characteristic peaks corresponding to different carbon bonding environments, including sp<sup>2</sup>-hybridized C-C (284.5 eV), C-O (285.7 eV), C=O (287.0 eV), and O-C=O (288.5 eV) bonds and the  $\pi$ - $\pi^*$  transition (~290.0 eV).<sup>36</sup> With increasing annealing temperature, a systematic reduction in the relative intensities of the peaks corresponding to the oxygen-containing functional groups (C-O, C=O, and O-C=O) was observed along with a notable enhancement of the sp<sup>2</sup>-hybridized C-C peak. This trend indicates the progressive removal of oxygen functionalities and an increase in graphitic ordering within the SWCNT framework. The improved structural order and diminished presence of surface oxygen species could also contribute to stronger electronic interactions between the SWCNT support and the Pt NPs, potentially influencing the catalytic behavior.

To investigate the structural changes in the SWCNTs in more detail, Raman spectroscopy was performed on pristine SWCNTs, acid-treated SWCNTs, and heat-treated SWCNTs. Fig. 5 shows the presence of characteristic D, G, and 2D bands in the Raman spectra of all samples. Specifically, the peaks at approximately 1350, 1580, and 2700 cm<sup>-1</sup> correspond to the D band (related to disorder and defects), the G band (sp2-carbon-

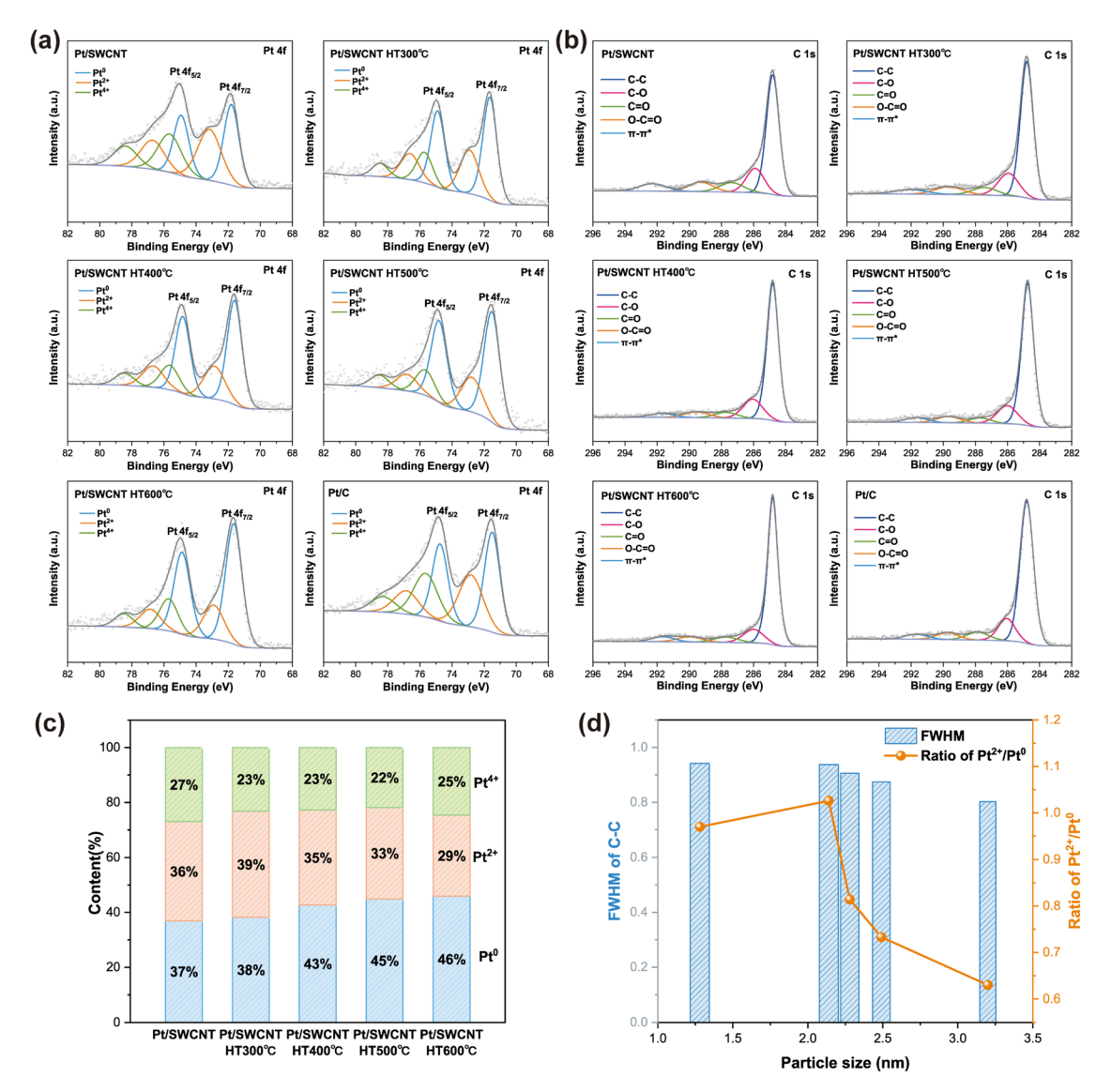


Fig. 4 (a) Pt 4f XPS spectra of Pt/SWCNT and commercial Pt/C. (b) C 1s XPS spectra of Pt/SWCNT and commercial Pt/C. (c) Content of Pt and oxidized Pt. (d) Changes in the Pt<sup>2+</sup>/Pt<sup>0</sup> ratio and FWHM of the C-C peak with the particle size.

like graphite), and the 2D band (secondary overtone of the D band). All spectra are normalized by the G-band intensity for an accurate comparison. The pristine SWCNTs showed a low ID/IG ratio of 0.025, indicating minimal defect density. Acid treatment increased the  $I_{\rm D}/I_{\rm G}$  ratio to  $\sim$ 0.099, confirming the introduction of defects. As the HT temperature increased, the  $I_{\rm D}/I_{\rm G}$ ratio initially rose to 0.118 for HT300 and subsequently decreased to 0.031 for HT600, indicating defect healing and improved graphitization in accordance with the C 1s XPS data.

Furthermore, after HT, the D-band shifted to lower wavenumbers and peak broadening was observed. This broadening indicates the overlap of vibrational components, which can be attributed to the change of point defects to more stable reconstituted defect structures (such as the Hecker-Elliott type topology) via thermal activation.<sup>37</sup>

Fig. 6 and Table S4 show the results of the evaluation of the ORR electrochemical activity. Fig. 6a and S1 display cyclic voltammograms (CVs) recorded in O2-saturated and N2-saturated

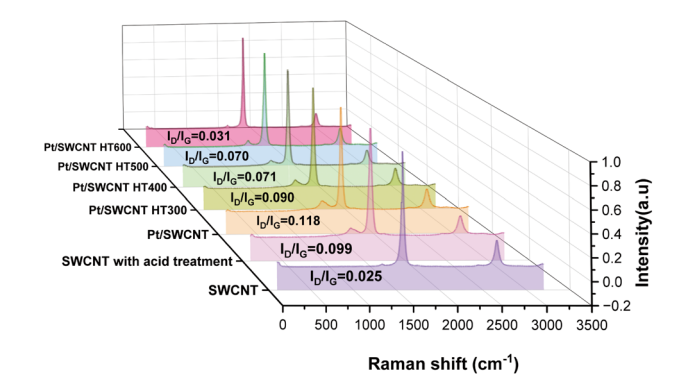


Fig. 5 Raman spectra of the SWCNT support before and after functionalization and subsequent heat treatments, illustrating the defect density changes  $(I_D/I_G \text{ ratios})$ .

0.1 M HClO<sub>4</sub> electrolyte, respectively. The CVs in the N<sub>2</sub>-saturated electrolyte show typical Pt features such as hydrogen adsorption/desorption and surface oxidation/reduction. In

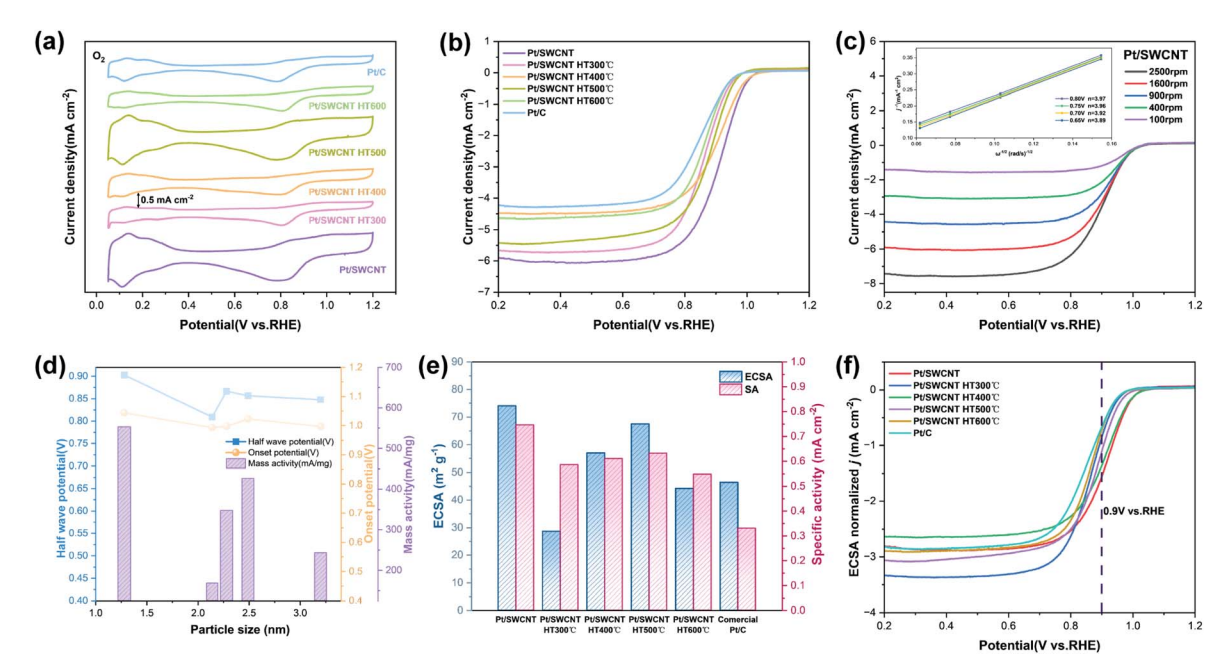


Fig. 6 Electrochemical performance of the Pt/SWCNT catalysts in 0.1 M HClO<sub>4</sub> solution: (a) cyclic voltammetry curves in O<sub>2</sub>-saturated solution, (b) linear sweep voltammetry curves in O2-saturated solution at 1600 rpm, (c) RDE polarization profiles of Pt/SWCNT at various rotation speeds and the respective Koutecky-Levich plots for different voltages, and (d) mass activity (mA mg<sup>-1</sup>-Pt) comparison as a function of the Pt nanoparticle size, (e) summary of ECSA and SA values for all catalysts, and (f) ECSA-normalized LSV curves.

contrast, the O<sub>2</sub>-saturated CV shows a pronounced cathodic current associated with the oxygen reduction reaction (ORR). The CV profiles exhibit characteristic redox features associated with the ORR dynamics for Pt/SWCNT and heat-treated Pt/ SWCNT. The large hysteresis between the cathodic and anodic sweeps ( $\Delta E > 200 \text{ mV}$ ) confirms the irreversible nature of the ORR under these conditions. The ORR performance was further evaluated by linear sweep voltammetry (LSV) measurements in an O<sub>2</sub>-saturated electrolyte at a scan rate of 10 mV s<sup>-1</sup> and a rotating disk electrode (RDE) speed of 1600 rpm.38 Fig. 6b shows the LSV profiles. Among the tested samples, the untreated Pt/SWCNT catalyst showed the best ORR performance, with an onset potential of 1.03 V vs. RHE and a half-wave potential of 0.90 V, both of which were superior to those of the heat-treated samples. Among the heat-treated samples, Pt/ SWCNT HT500 exhibited the highest ORR activity but lower half-wave potential and MA (426.6 mA mg<sup>-1</sup>) than Pt/SWCNT. To accurately determine the electron transfer number in the ORR on the Pt/SWCNT catalysts, a Koutecky-Levich analysis was performed using LSV while varying the rotation speed of the RDE.<sup>39</sup> As shown in Fig. 6c, the electron transfer number is in the range of 3.89-3.98, suggesting that the ORR mainly follows the four-electron transfer pathway. This observation is consistent with previous studies on Pt-based electrocatalysts, for which the four-electron pathway has been reported as the dominant mechanism under similar experimental conditions. Fig. 6d shows the obtained onset potentials, half-wave potentials, and MAs, highlighting the discontinuity around the critical size of 1.5 nm where the classical scaling breaks down and marks the beginning of a remarkable catalytic enhancement at the quantum scale (~1 nm).11,16,31 As shown in Fig. 6e, the

untreated Pt/SWCNT catalyst exhibited the highest ECSA ( $\sim$ 74  $m^2$   $g^{-1}$ ) and SA ( $\sim 0.73$  mA cm<sup>-2</sup>), indicating excellent Pt dispersion and surface accessibility. Heat treatment led to a general decline in both metrics. Among treated samples, Pt/ SWCNT HT500 retained a relatively high ECSA and SA, suggesting a balance between enhanced conductivity and preserved structure. To compare intrinsic catalytic activities, the ORR polarization curves were normalized by the ECSA (Fig. 6f). The untreated Pt/SWCNT catalyst exhibited the highest specific activity, with the most negative normalized current density at 0.9 V vs. RHE. This trend is consistent with its superior onset potential (1.03 V) and half-wave potential (0.90 V) in the nonnormalized LSV profiles (Fig. 6b), suggesting not only a higher density of active sites but also more efficient site utilization. The ECSA-normalized analysis corroborates the previously observed deviation from classical scaling (Fig. 6d).

This enhancement in the catalytic activity is mainly attributed to two key factors: (i) the dominant presence of catalytically favorable low-coordination sites such as edges and corners and (ii) electronic discretization stemming from quantum confinement. Extended Pt 111 terraces are typically less active toward the ORR, whereas ultrasmall Pt NPs are structurally dominated by undercoordinated sites with higher intrinsic reactivity. This interpretation is in agreement with experimental and theoretical studies. For example, Shao et al. showed that although small particles offer high dispersion, excessively strong oxygen binding at edge sites ( $\Delta GO^* = -1.4 \text{ eV}$ ) can limit the activity.<sup>16</sup> In contrast, Pt 111 shows moderate adsorption ( $\Delta GO^*$  from -0.7 to -0.8 eV) but lower intrinsic activity owing to a limited number of undercoordinated sites. Garlyyev et al. showed that  $\sim$ 1.1-nm NPs exhibit optimal GCN (7.5–8.3) distributions with MA nearly 10 times higher than that of Pt 111 because of the presence of partially undercoordinated sites. 11 Hoshi et al. also showed that Pt 111 suffers from OH\* poisoning, which suppresses activity unless modified, highlighting the importance of surface state tuning.31 These results support the notion that quantum-scale Pt particles exhibit discrete reactivity profiles that cannot be explained solely by classical scaling relations. Recent work by Ohnuma et al. further highlighted that for Pt<sub>3-9</sub> clusters supported on graphene, the experimentally observed ORR activity deviates from trends predicted by simple d-band center theory, suggesting a breakdown of conventional scaling relationships at the quantum cluster scale.28

The present experimental data provide compelling evidence that the ORR activity in Pt NPs is not solely a function of the particle size but a complex interplay between the geometric structure, coordination environment, and quantum confinement-induced electronic modulation. Although the enhanced performance of the  $\sim$ 1.0-nm Pt/SWCNT catalysts may initially appear to contradict previous reports suggesting that the activity reaches a maximum at ~2.2 nm,16 these observations are actually complementary, rooted in different catalytic mechanisms that become dominant at different size regimes.

At the ~1.0 nm scale, Pt NPs enter the quantum-confined regime, where discrete electronic states and reduced symmetry profoundly alter the surface electronic density of states. This results in a shift of the d-band center and a departure from bulk scaling features. In particular, these ultrasmall clusters are structurally dominated by undercoordinated surface atoms, e.g., with coordination numbers (CNs) of 5-7, which serve as highly active adsorption sites for O2 and its intermediates. Moreover, DFT studies have shown that such clusters exhibit broadened and discretized d-bands, leading to modulated  $\Delta GO^*$  and  $\Delta GOH^*$  values that deviate from those of extended Pt 111 and larger NP surfaces.21,22 The deviation from the classical volcano-type activity trend, which is observed experimentally as a discontinuous jump in MA at the 1.5 nm threshold (Fig. 6d), is thus consistent with a transition to this quantum-confined regime. Notably, the enhanced ORR activity of these ~1.0 nm Pt nanoparticles persists even when the average interparticle distance falls below 1 nm. This behavior contrasts with that observed on glassy carbon electrodes (GCEs), where overlapping electric double layers (EDLs) were proposed to modulate local potential distributions.40 In our system, however, the high electrical conductivity of the SWCNT support likely ensures a more uniform potential landscape, independent of EDL overlap, thereby stabilizing the electrochemical environment even at sub-nanometer spacing. Moreover, Imaoka et al. demonstrated that the ORR activity of dendrimer-stabilized Pt clusters varies non-monotonically with atomicity, with Pt<sub>19</sub> showing a distinct maximum due to edgerich geometries and orbital localization.41

In contrast, the previously reported activity maximum around 2.2 nm corresponds to the emergence of truncated octahedral or cuboctahedral crystalline structures with highly coordinated (CN > 8) terrace atoms but an optimized distribution of edge and corner sites. In this size range, Pt NPs maintain sufficient surface curvature to enhance the reactivity while avoiding excessive OH\*

binding energy penalties, which are common in smaller clusters. This balance results in a Sabatier-optimal intermediate adsorption strength. Thus, the activity of 2.2 nm particles stems from geometric optimization and favourable CN distributions, 11,16 whereas that of  $\sim$ 1 nm particles can be ascribed to quantum modulation and the prevalence of highly active edge-dominated surface morphologies.

Our XRD and TEM results further support this interpretation: the as-synthesized Pt/SWCNT samples exhibit broad 111 reflections and high  $I_{111}/I_{200}$  (Fig. 3), indicating structural disorder and a dominance of noncrystalline or amorphous motifs, which are often associated with low-coordination, highly reactive sites. The high degree of XRD broadening (FWHM = 2.48°) is characteristic of ultrasmall clusters with strong lattice distortions, as previously reported for quasiamorphous Pt NPs in the sub-1.5 nm regime.32 As the particle size increased with HT, both the reflectance and  $I_{111}/I_{200}$ approach bulk values, indicating structural ordering and a concomitant loss of the quantum-confined structural state. Crucially, the lack of a direct correlation between the oxidation state and the ORR performance (Fig. 6c and d) underscores that the catalytic performance is primarily determined by structural and electronic factors rather than only surface chemical species. In fact, the highest MA (552.9 mA mg<sup>-1</sup>) is observed for the sample with the lowest Pt<sup>0</sup> content, confirming that the oxidation state alone is not a reliable descriptor of the performance in this quantum size regime. Taken together, these results indicate that quantum-confined Pt NPs (<1.5 nm) access a distinct catalytic landscape characterized by undercoordination, d-band discretization, and nonbulk morphologies, moving beyond traditional design paradigms based on scaling relationships.

To evaluate the electrochemical durability of the Pt/SWCNT catalyst, accelerated stress tests (ASTs) were carried out over 2000 potential cycles between 0.6 and 1.0 V (vs. RHE) in O2-saturated 0.1 M HClO<sub>4</sub>. As shown in Fig. 7a and b, CV profiles recorded in N2- and O2-saturated electrolytes show attenuated hydrogen adsorption/desorption and oxygen reduction peaks after cycling, indicating a partial loss of the electrochemically active surface area (ECSA). The LSV curve (Fig. 7c) exhibits a slight negative shift in the half-wave potential, suggesting minor degradation in oxygen reduction reaction (ORR) kinetics. Quantitative comparisons of the ECSA and catalytic activity before and after cycling (Fig. 7d) demonstrate the remarkable electrochemical durability of the Pt/ SWCNT catalyst under AST conditions. The modest decline in SA (~9.5%) indicates that the intrinsic catalytic performance of the remaining Pt surface is well retained, while the minimal losses in MA ( $\sim$ 14%) and ECSA ( $\sim$ 5.3%) further underscore the robustness of the catalyst. As shown in Fig. 7e, Pt nanoparticles remain uniformly dispersed on the SWCNT surface with no significant aggregation or detachment. Particle size analysis (Fig. 7f) shows that 77.78% of the particles remain below 1.5 nm, with an average diameter of 1.35 nm, compared to 1.28 nm before cycling. This slight increase indicates that SWCNTs effectively anchor Pt nanoparticles, limiting their mobility and mitigating electrochemical stress.

Fig. 8 and Table S5 show the fuel cell performance of membrane electrode assemblies (MEAs) constructed using the

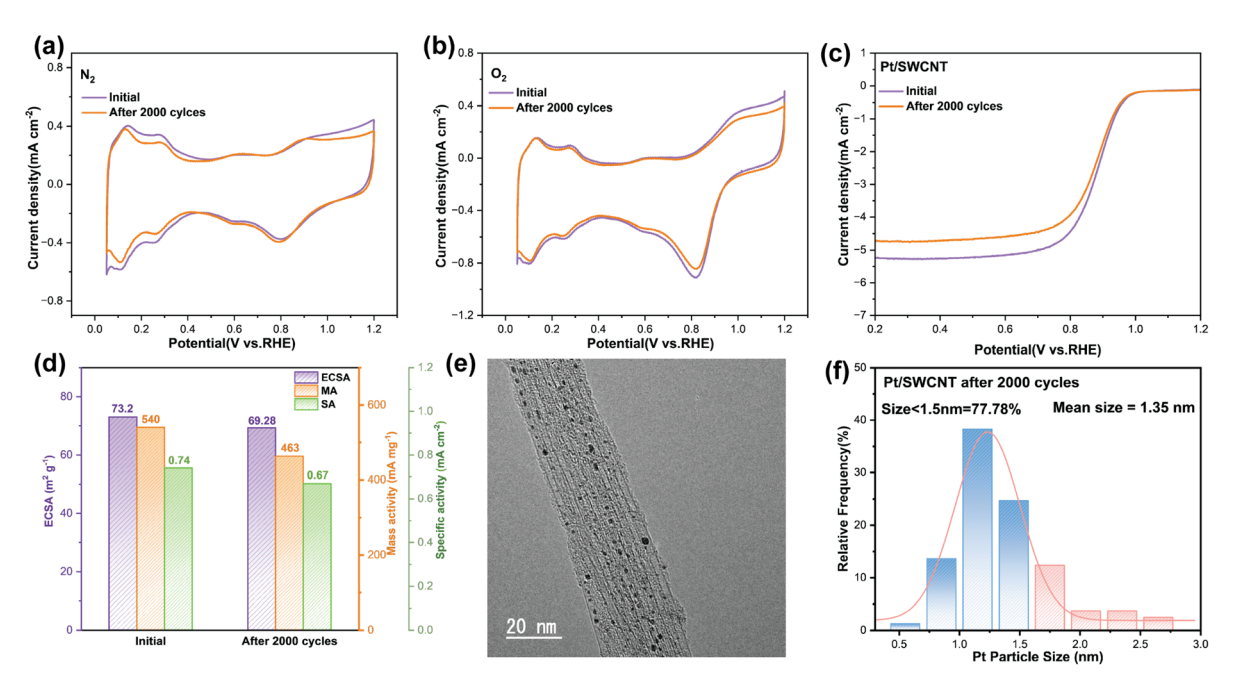


Fig. 7 Electrochemical and structural characterization of Pt/SWCNT catalysts before and after accelerated stress testing (AST). (a and b) CV curves in  $N_2$ - (a) and  $O_2$ -saturated (b)  $0.1 \, M \, HClO_4$  at a scan rate of 50 mV s<sup>-1</sup>. (c) LSV curves under  $O_2$ -saturated 0.1 M  $HClO_4$  at a rotation rate of 1600 rpm. (d) Electrochemically derived ECSA, MA and SA values before and after AST. (e) TEM image of the Pt/SWCNT catalyst after AST. (f) Particle size distribution histogram of Pt nanoparticles after AST.

Pt/SWCNT catalysts. The MEA based on the untreated Pt/SWCNT catalyst exhibited a high current density of 594.3 mA cm $^{-2}$  at 0.6 V and a peak power density of 660.4 mW cm $^{-2}$ . The Pt/SWCNT HT500–based MEA showed slightly improved performance (639.7 mA cm $^{-2}$  and 680.1 mW cm $^{-2}$ ), likely due to the improved electrode morphology, which partially compensates for the reduced quantum effects caused by particle growth. In contrast, the commercial Pt/C–based MEA delivered a much lower current density of 272.8 mA cm $^{-2}$  at 0.6 V and a peak power density of 491.1 mW cm $^{-2}$ , clearly demonstrating the superior fuel cell performance of the Pt/SWCNT catalysts under identical testing conditions.

These results suggest that the superior ORR activity of  $\sim$ 1 nm Pt NPs results from a synergistic combination of abundant low-coordination surface sites, quantum confinement-induced modulation of electronic states, and optimized adsorption energetics. These quantum structural and electronic effects override the classical size–activity trends, establishing a new design principle.

To deepen our understanding of the observed size-activity transition, we evaluated the structural evolution of Pt NPs in terms of magic numbers and crystal habits. The geometry, coordination, and ORR-relevant features of Pt NP clusters are summarized schematically in Fig. 9 and Table S6. Magic

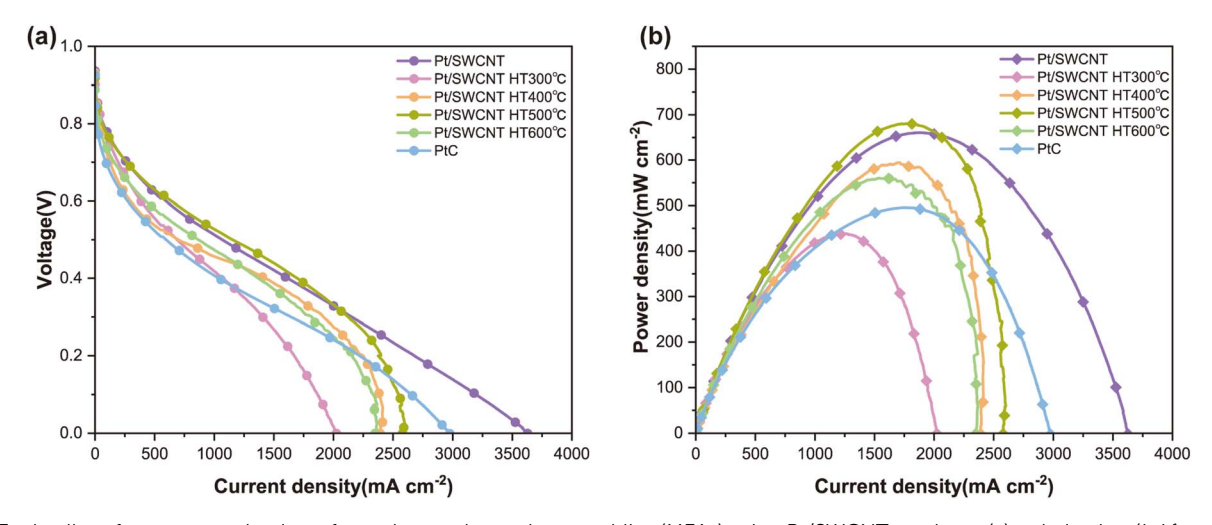


Fig. 8 Fuel cell performance evaluation of membrane electrode assemblies (MEAs) using Pt/SWCNT catalysts: (a) polarization (I-V) curves and (b) power density curves of the Pt/SWCNT catalysts and commercial Pt/C benchmark catalysts.

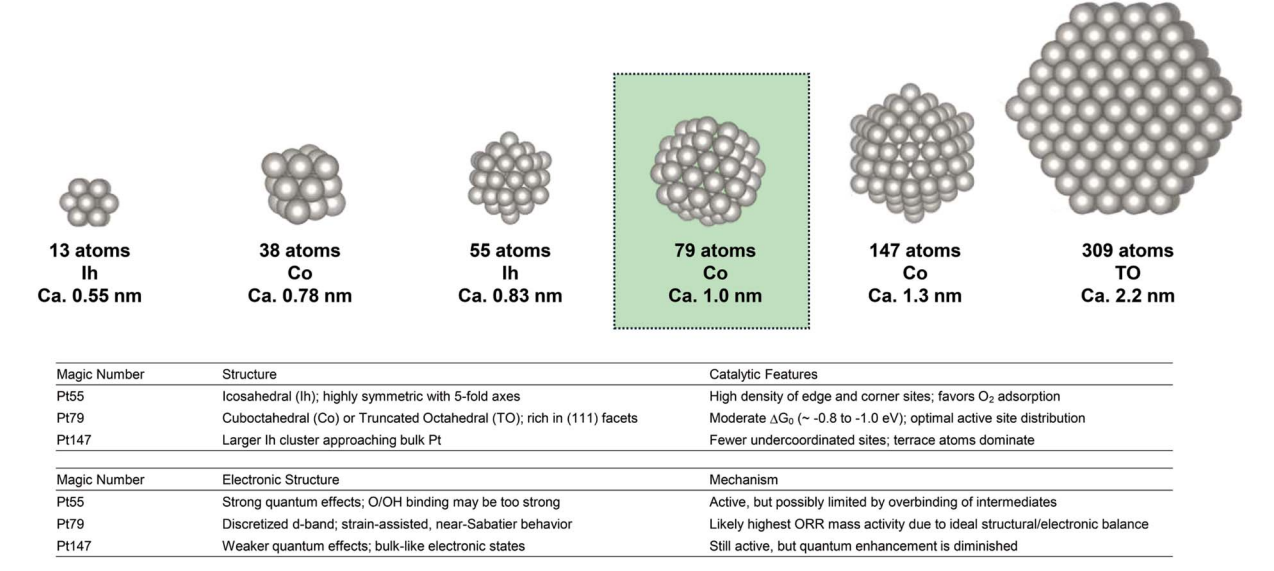


Fig. 9 Structural motifs and ORR-relevant properties of Pt magic number clusters. Schematic comparing the geometry, coordination environments, and oxygen adsorption energetics of Pt55 (Ih), Pt79 (Co/TO), and Pt147 (Co) clusters. Pt79 exhibits the highest ORR mass activity due to an optimal balance between low-coordination surface atoms and moderated  $\Delta GO^*$  values (from -0.8 to -1.0 eV), consistent with the quantum confinement and Sabatier principles.

number clusters—those with specific atomic numbers such as 13, 38, 55, 79, 147, and 309—correspond to complete shells of highly symmetric motifs, including icosahedral (Ih), cuboctahedral (Co), and truncated octahedral (TO) geometries. These configurations are not only structurally favored owing to surface energy minimization but also exhibit unique electronic properties that profoundly affect the catalytic performance, as demonstrated by the DFT global optimization studies reported by Liu and Wei. 42 For example, the 13-atom Ih cluster (~0.5 nm diameter) represents the minimal closed-shell structure with high symmetry and exhibits pronounced quantum effects. The next relevant magic number is 55, with the fivefold symmetry of the 55-atom Ih cluster (~0.83 nm) maximizing the surface-tovolume ratio and undercoordination. Both clusters are known to have a high density of corner and edge atoms, favoring O<sub>2</sub> adsorption.

As the number of atoms increases, structures such as the 79atom Co cluster ( $\sim$ 1.0 nm) and the 147-atom Ih cluster ( $\sim$ 1.3 nm) become relevant. These geometries exhibit intermediate GCNs, typically between 7.5 and 8.3, especially for atoms located on (111) terraces and facet junctions. Garlyyev et al.11 highlighted that Pt clusters with a size of around 1.1 nm exhibit enhanced ORR activity owing to the optimal balance between activity and stability provided by this GCN distribution.

Interestingly, our study reveals a nonmonotonic trend in the ORR MA with decreasing Pt NP diameter. The MA decreases between 2.5 and 1.5 nm but unexpectedly recovers at  $\sim$ 1.0 nm, which corresponds to the size of magic number clusters such as those containing 55 and 79 atoms. This behavior cannot be explained by conventional size-scaling theories. Similar deviations from monotonic activity trends have been reported for Au magic number clusters in the 1-3.5 nm range, 43 supporting that quantum confinement can override classical geometrical

scaling. Instead, this size constitutes a transition point where quantum confinement induces d-band discretization, alters adsorption energetics, and stabilizes active nonmetallic motifs. XRD data support this structural interpretation: the 111 reflection in  $\sim$ 1.0 nm samples is considerably broadened (FWHM = 2.48°), indicating lattice distortion rather than disorder. The  $I_{(111)}/I_{(200)}$  value of  $\sim$ 9.6, which far exceeds that of bulk Pt ( $\sim$ 2.0), is characteristic of structures rich in (111) facets or partially amorphous shells with short-range order, such as truncated icosahedra or defective Ih clusters.21,32

Furthermore, TEM and statistical analyses showed that nearly 81% of the particles in the as-synthesized Pt/SWCNT samples are <1.5 nm, with the mean size centered at  $\sim$ 1.28 nm. According to atomic packing models, this corresponds to clusters of 38-79 atoms, which are associated with enhanced ORR in the quantum regime. These sizes are consistent with magic number structures characterized by high surface atom fraction and edge/corner site density, which enhance the ORR kinetics.

The electrochemical measurements support this conclusion: the MA of  $\sim$ 1.0 nm NPs reached 552.9 mA mg<sup>-1</sup>, outperforming even the Pt/SWCNT HT500 sample with larger quantum clusters, which exhibited site-specific ΔGO\* values ranging from -0.8 to -1.3 eV due to low coordination environments. Previous DFT calculation studies confirmed that such edge- and defectrich sites can promote O2 activation despite excessive binding, especially when surface disorder breaks scaling constraints.21,22

In contrast, the optimal activity around 2.2 nm previously reported by Shao et al. 16 results from the geometric optimization of well-defined facets with favorable curvature, edge-to-terrace ratios, and minimal strain. Thus, the enhanced performance of 1.0-nm and 2.2-nm catalysts stems from different mechanisms, i.e., the former is governed by the quantum structure and electronic discretization and the latter by the crystalline geometry and GCN tuning.

Taken together, these results suggest that the nanoscale electrocatalytic behavior stems from a combination of magic number-induced stability, coordination environment, crystal habit (e.g., Ih, TO, and Co), and quantum modulation of the surface electronic structure rather than traditional monotonic trends, which will lead to the development of a new electrocatalyst design principle based on quantum structure engineering.

# 3. Conclusion

We demonstrated a controlled solution plasma synthesis method that enables the fabrication of monodisperse, quantum-sized ( $\sim$ 1.0 nm) Pt NPs supported on SWCNTs. The ORR activity of the resulting Pt/SWCNT catalysts exhibited a quantum-induced discontinuity with a pronounced transition occurring near 1.5 nm. Below this critical threshold, the classical size-scaling relations no longer apply; instead, the catalytic behavior is governed by quantum confinement through discrete electronic states, modulated adsorption energetics, and structurally disordered motifs.

Comprehensive structural, spectroscopic, and electrochemical analyses confirmed the emergence of a distinct quantum-confined regime below 1.5 nm. The observed enhancement in the ORR activity at  $\sim$ 1.0 nm is attributed to a synergistic interplay between low-coordination active sites and d-band discretization effects.<sup>44</sup> Notably, this enhancement corresponds to magic number clusters such as Pt<sub>55</sub> and Pt<sub>79</sub>, which feature closed-shell configurations with exceptional structural and electronic stability.<sup>45</sup> XRD peak broadening and elevated  $I_{111}/I_{200}$  indicate the existence of nonbulk crystal habits—Ih, TO, or Co—that enhance edge and corner site density, induce lattice strain, and promote dorbital localization.<sup>46</sup> These features reinforce the view that reactivity in the sub-1.5 nm regime is dictated by a confluence of geometry, coordination, and quantum electronics instead of by facet-dependent scaling.

This work delineates the boundary between classical and quantum electrocatalysis and advances a design strategy that embraces, rather than circumvents, quantum effects. Tailored nanoclusters engineered in terms of size, symmetry, and crystallographic habit offer a viable path toward next-generation fuel cell catalysts with enhanced efficiency and reduced Pt loading.

# 4. Experimental section

#### 4.1 Materials

SWCNTs with  $\geq$ 98% purity and diameters of 2–3 nm (EC2.0P) were purchased from Meijo Nanocarbon Co. Ethanol ( $\geq$ 99.5%) and 2-propanol (IPA,  $\geq$ 99.7%) were obtained from Kanto Chemical Co. Platinum chloride hydrate ( $H_2PtCl_6 \cdot 6H_2O$ ,  $\geq$ 99.9%) and 5 wt% Nafion solution were purchased from Sigma-Aldrich (USA). Tungsten rods (1.0 mm diameter,  $\geq$ 99.99%) were purchased from Nilaco (Japan). PTFE membrane filters (0.1  $\mu$ m) were purchased from Merck (USA).

Commercial 20 wt% Pt/C and 46 wt% Pt/C catalysts were obtained from Sigma-Aldrich and the Tanaka Kikinzoku Group, respectively. Perchloric acid (70%  $\rm HClO_4$ ), nitric acid (65%  $\rm HNO_3$ ), and sulfuric acid (98%  $\rm H_2SO_4$ ) were obtained from Kanto Chemical. All reagents were of analytical grade and used as received. The used chemicals are listed in Table S1.

#### 4.2 Functionalization of SWCNTs

The as-received SWCNTs were first oxidized in air at  $500\,^{\circ}\text{C}$  for 2 h to remove amorphous carbon and open the nanotube ends and then refluxed in a  $3:1\,(\text{v/v})$  mixture of concentrated sulfuric and nitric acids at  $120\,^{\circ}\text{C}$  for 3 h to remove the residual catalyst and carbonaceous impurities while introducing oxygencontaining functional groups onto the SWCNT surface. The modified SWCNTs were washed with deionized water until the effluent reached neutral pH and dried at  $80\,^{\circ}\text{C}$  for  $10\,\text{h}$ .

#### 4.3 Preparation of Pt/SWCNT catalysts

The Pt/SWCNT catalysts were synthesized using a solution plasma method, as schematically illustrated in Fig. 1. The solution plasma conditions are listed in Table S2. Two tungsten wire electrodes (1 mm diameter) were wound around an insulating ceramic tube, leaving a 1 mm gap, and placed in a glass reactor containing 100 mL of 1 mM H<sub>2</sub>PtCl<sub>6</sub>·6H<sub>2</sub>O in a 90: 10 (v/ v) water/ethanol solution. Plasma was generated at atmospheric pressure with a bipolar pulse power supply (Kurita Mfg. Co., Japan). The pulse width, frequency, and discharge voltage were 1.5 µs, 30 kHz, and 2.4 kV, respectively. After 10 min of discharge, a dark-brown colloidal suspension of Pt NPs was formed. In parallel, 20 mg of untreated SWCNTs were dispersed in 100 mL of ethanol via ultrasonication for 30 min. This SWCNT suspension was then added to the Pt colloid, and the mixture was continuously sonicated and stirred for ~12 h to facilitate Pt NP deposition. The resulting Pt/SWCNT composite was collected via vacuum filtration using a 0.1 μm PTFE membrane, washed thoroughly with distilled water, and vacuum dried at 80 °C for 3 h. Finally, the composite was heattreated under a H<sub>2</sub>-Ar gas flow for 2 h at controlled temperatures (300-600 °C).

#### 4.4 Characterization

High-resolution transmission electron microscopy (TEM) was performed on a JEM-2100F microscope (JEOL) operated at 200 kV. Samples were prepared by sonicating the Pt/SWCNT powders in ethanol and drop-casting the suspension onto a TEM grid. Thermogravimetric analysis (TGA) was conducted in air from room temperature to  $1000\,^{\circ}$ C at a heating rate of  $10\,^{\circ}$ C min<sup>-1</sup> to estimate the Pt mass fraction. X-ray photoelectron spectroscopy (XPS) was conducted to determine the oxidation state of Pt deposited on the supports of the catalysts using an ESCALAB 250Xi spectrometer (Thermo Fisher Scientific) with Mg Kα radiation as the X-ray source. The spectra were recorded with a pass energy of 20 eV and an acquisition step size of 0.5 eV. X-ray diffraction (XRD) analysis was conducted to assess the crystallinity of the catalyst using a SmartLab diffractometer (Rigaku) with Cu Kα radiation, operating at 45 kV and 200 mA.

The diffraction patterns were recorded over a  $2\theta$  range of 20–80° at a scan speed of 1.5° min<sup>-1</sup> with a step size of 0.02°.

#### 4.5 Electrochemical characterization

The electrochemical performance of the Pt/SWCNT catalysts subjected to different thermal treatments was evaluated using a Biologic VSP electrochemical workstation. All measurements were conducted in a conventional three-electrode system at 20 °C in 0.1 M HClO<sub>4</sub> solution. A glassy carbon rotating disk electrode (RDE, HAG1512m/BP, Hokuto Denko, Japan) with a geometric surface area of 0.196 cm<sup>2</sup> was used as the working electrode, Pt foil served as the counter electrode, and a reversible hydrogen electrode (RHE) was used as the reference electrode. The catalyst ink was prepared by dispersing a certain amount of catalyst based on the Pt loading percentage in a mixture of 0.75 mL IPA, 1.25 mL distilled water, and 15 µL Nafion solution (5 wt%). The suspension was ultrasonicated for 30 min to ensure uniform dispersion. Then, 10  $\mu$ L of the ink was drop-cast onto the polished RDE surface, achieving a Pt loading of approximately 8 μg cm<sup>-2</sup>. The electrode was dried under ambient conditions before immersion in the electrolyte solution. Prior to the electrochemical measurements, the electrolyte solution was purged with nitrogen gas for 30 min to remove dissolved O2. Cyclic voltammetry (CV) was performed in N2-saturated 0.1 M HClO4 solution using a scan rate of 50 mV s<sup>-1</sup> over a potential range of 0.04–1.2 V (vs. RHE). The oxygen reduction reaction (ORR) activity was assessed via linear sweep voltammetry (LSV) in O2-saturated 0.1 M HClO4 solution. LSV measurements were conducted at a rotation speed of 1600 rpm over a potential range of 0.2-1.2 V (vs. RHE) with a scan rate of 10 mV  $s^{-1}$ .

#### 4.6 Fuel cell performance evaluation

Membrane electrode assemblies (MEAs) were fabricated to assess the practical fuel cell performance (Fig. S2). The cathode catalyst ink was prepared by dispersing Pt/SWCNT in water and IPA, followed by the addition of a 20 wt% Nafion solution. For comparison, a commercial Pt/C catalyst ink was prepared in a similar manner. The ink was cast to a PTFE film using the doctor-blade method and dried at 120 °C for 2 h, targeting a Pt loading of 0.15 mg Pt cm $^{-2}$ . The MEA was then formed  $\nu ia$  the hot-pressing process at 140 °C for 3 min by applying a pressure of 1.5 MPa on the cathode, anode, and Nafion membrane. The fuel cell performance was evaluated at 80 °C under fully humidified  $\rm H_2$  and air streams using a Biologic VMP-300 instrument to record the polarization ( $\it I-V$ ) and CV curves.

## **Author contributions**

Zhuoya Deng: conducted the experiments, analysed the data, and wrote the manuscript. Yuanyuan Liu: assisted with experimental design and data interpretation. Pengfei Wang and Zhunda Zhu: contributed to materials synthesis and characterization. Nutthira Pakkang, Garbis Atam Akceoglu, and Sangwoo Chae: discussed the results and reviewed the manuscript. Yasuyuki Sawada: supervised the project and revised the

manuscript. Nagahiro Saito: supervised the research, reviewed and edited the manuscript and acquired funding.

#### Conflicts of interest

The authors declare that there are no competing interests.

# Data availability

The data are available from the corresponding author upon reasonable request.

CV curves of Pt/SWCNT catalysts in  $N_2$ -saturated 0.1 M  $HClO_4$  solution; schematic of MEA configuration; summary of materials used, including supplier information and purity grades; experimental conditions for the synthesis of catalysts; average particle diameter, interparticle spacing, and particle size distributions derived from the TEM analysis; summary of electrochemical parameters obtained from the CV and ORR tests; and maximum power density and current density at 0.6 V from MEA test. See DOI: https://doi.org/10.1039/d5ta04934b.

# Acknowledgements

This study is partially based on results obtained from projects JPNP20003, commissioned by the New Energy and Industrial Technology Development Organization (NEDO), Japan, JPMJPF2204 commissioned by the Japan Science and Technology Agency (JST), Japan, and JPJ012308 commissioned by the Council for Science, Technology and Innovation (CSTI), Japan. Zhuoya Deng also acknowledges financial support from the China Scholarship Council (No. 202308050114).

#### References

- L. Yang, J. Shui, L. Du, Y. Shao, J. Liu, L. Dai and Z. Hu, Adv. Mater., 2019, 31, 1804799.
- 2 X. Wang, Z. Li, Y. Qu, T. Yuan, W. Wang, Y. Wu and Y. Li, *Chem*, 2019, 5, 1486–1511.
- 3 Y. Li, Q. Li, H. Wang, L. Zhang, D. P. Wilkinson and J. Zhang, *Electrochem. Energy Rev.*, 2019, **2**, 518–538.
- 4 Y. Nie, L. Li and Z. Wei, Chem. Soc. Rev., 2015, 44, 2168-2201.
- 5 Q. Xue, Z. Wang, Y. Ding, F. Li and Y. Chen, *Chin. J. Catal.*, 2023, **45**, 6–16.
- 6 R. Cui, L. Mei, G. Han, J. Chen, G. Zhang, Y. Quan, N. Gu, L. Zhang, Y. Fang, B. Qian, X. Jiang and Z. Han, *Sci. Rep.*, 2017, 7, 41826.
- 7 M. Shao, Q. Chang, J.-P. Dodelet and R. Chenitz, *Chem. Rev.*, 2016, 116, 3594–3657.
- 8 W. Yu, M. D. Porosoff and J. G. Chen, *Chem. Rev.*, 2012, **112**, 5780–5817.
- 9 W. Xiao, M. A. L. Cordeiro, M. Gong, L. Han, J. Wang, C. Bian, J. Zhu, H. L. Xin and D. Wang, *J. Mater. Chem. A*, 2017, 5, 9867–9872.
- 10 V. Viswanathan and F. Y.-F. Wang, *Nanoscale*, 2012, **4**, 5110–5117
- 11 B. Garlyyev, K. Kratzl, M. Rück, J. Michalička, J. Fichtner, J. M. Macak, T. Kratky, S. Günther, M. Cokoja,

- A. S. Bandarenka, A. Gagliardi and R. A. Fischer, *Angew. Chem.*, *Int. Ed.*, 2019, **58**, 9596–9600.
- 12 M. Rück, A. Bandarenka, F. Calle-Vallejo and A. Gagliardi, *J. Phys. Chem. Lett.*, 2018, **9**, 4463–4468.
- 13 V. Tripković, I. Cerri, T. Bligaard and J. Rossmeisl, *Catal. Lett.*, 2014, 144, 380–388.
- 14 H. Yano, J. Inukai, H. Uchida, M. Watanabe, P. K. Babu, T. Kobayashi, J. H. Chung, E. Oldfield and A. Wieckowski, *Phys. Chem. Phys.*, 2006, **8**, 4932–4939.
- 15 G. A. Tritsaris, J. Greeley, J. Rossmeisl and J. K. Nørskov, *Catal. Lett.*, 2011, **141**, 909–913.
- 16 M. Shao, A. Peles and K. Shoemaker, *Nano Lett.*, 2011, 11, 3714–3719.
- 17 S. Proch, M. Wirth, H. S. White and S. L. Anderson, *J. Am. Chem. Soc.*, 2013, **135**, 3073–3086.
- 18 I. E. L. Stephens, J. Rossmeisl and I. Chorkendorff, *Science*, 2016, 354, 1378–1379.
- 19 M. Inaba, A. Zana, J. Quinson, F. Bizzotto, C. Dosche, A. Dworzak, M. Oezaslan, S. B. Simonsen, L. T. Kuhn and M. Arenz, ACS Catal., 2021, 11, 7144–7153.
- 20 M. Imada, A. Fujimori and Y. Tokura, *Rev. Mod. Phys.*, 1998, 70, 1039–1263.
- 21 L. Li, L.-L. Wang, D. D. Johnson, Z. Zhang, S. I. Sanchez, J. H. Kang, R. G. Nuzzo, Q. Wang, A. I. Frenkel, J. Li, J. Ciston, E. A. Stach and J. C. Yang, *J. Am. Chem. Soc.*, 2013, 135, 13062–13072.
- 22 R. Wang, D. Chen, L. Fang, W. Fan, Q. You, G. Bian, Y. Zhou, W. Gu, C. Wang, L. Bai, J. Li, H. Deng, L. Liao, J. Yang and Z. Wu, *Angew. Chem., Int. Ed.*, 2024, 63, e202402565.
- 23 H. Li, K.-W. Wang, A. Hu, J.-P. Chou and T.-Y. Chen, *Phys. Chem. Chem. Phys.*, 2021, 23, 18012–18025.
- 24 B. Qiao, A. Wang, X. Yang, L. F. Allard, Z. Jiang, Y. Cui, J. Liu, J. Li and T. Zhang, *Nat. Chem.*, 2011, 3, 634–641.
- 25 L. Lu, S. Zou and B. Fang, ACS Catal., 2021, 11, 6020-6058.
- 26 Z. Zhang, C. Feng, C. Liu, M. Zuo, L. Qin, X. Yan, Y. Xing, H. Li, R. Si, S. Zhou and J. Zeng, *Nat. Commun.*, 2020, 11, 1215.
- 27 L. Liu, S. Liu, L. Li, H. Qi, H. Yang, Y. Huang, Z. Wei, L. Li, J. Xu and B. Liu, J. Mater. Chem. A, 2020, 8, 6190–6195.

- 28 A. Ohnuma, K. Takahashi, H. Tsunoyama, T. Inoue, P. Zhao, A. Velloth, M. Ehara, N. Ichikuni, M. Tabuchi and A. Nakajima, Catal. Sci. Technol., 2022, 12, 1400–1407.
- 29 J. Clavilier, D. Armand, S. G. Sun and M. Petit, *J. Electroanal. Chem. Interfacial Electrochem.*, 1986, 205, 267–277.
- 30 N. Hoshi, Mater. Jpn., 2020, 59, 379-386.
- 31 N. Hoshi, M. Nakamura, R. Kubo and R. Suzuki, *Commun. Chem.*, 2024, 7, 1–7.
- 32 D. E. Ramaker, M. K. Oudenhuijzen and D. C. Koningsberger, *J. Phys. Chem. B*, 2005, **109**, 5608–5617.
- 33 F. Qian, L. Peng, Y. Zhuang, L. Liu and Q. Chen, *Chin. J. Chem. Eng.*, 2023, **61**, 140–146.
- 34 G. Liu, R. Luo, J. Ma, T. Guo, J. Kang, W. Shi, W. Zhou and L. Guo, Angew. Chem., 2025, 137, e202422199.
- 35 A. K. Shukla, A. S. Aricò, K. M. El-Khatib, H. Kim, P. L. Antonucci and V. Antonucci, *Appl. Surf. Sci.*, 1999, 137, 20–29.
- 36 J.-H. Zhou, Z.-J. Sui, J. Zhu, P. Li, D. Chen, Y.-C. Dai and W.-K. Yuan, *Carbon*, 2007, 45, 785–796.
- 37 S. Saito and I. Tomita, Mater. Res. Express, 2020, 7, 056301.
- 38 K. J. J. Mayrhofer, D. Strmcnik, B. B. Blizanac, V. Stamenkovic, M. Arenz and N. M. Markovic, *Electrochim. Acta*, 2008, **53**, 3181–3188.
- 39 D. Wang, H. L. Xin, R. Hovden, H. Wang, Y. Yu, D. A. Muller, F. J. DiSalvo and H. D. Abruña, *Nat. Mater.*, 2013, **12**, 81–87.
- 40 M. Nesselberger, M. Roefzaad, R. Fayçal Hamou, P. Ulrich Biedermann, F. F. Schweinberger, S. Kunz, K. Schloegl, G. K. H. Wiberg, S. Ashton, U. Heiz, K. J. J. Mayrhofer and M. Arenz, *Nat. Mater.*, 2013, 12, 919–924.
- 41 T. Imaoka, H. Kitazawa, W.-J. Chun and K. Yamamoto, *Angew. Chem., Int. Ed.*, 2015, **54**, 9810–9815.
- 42 G.-F. Wei and Z.-P. Liu, Chem. Sci., 2015, 6, 1485-1490.
- 43 H. Li, L. Li, A. Pedersen, Y. Gao, N. Khetrapal, H. Jónsson and X. C. Zeng, *Nano Lett.*, 2015, **15**, 682–688.
- 44 J. Aarons, L. Jones, A. Varambhia, K. E. MacArthur, D. Ozkaya, M. Sarwar, C.-K. Skylaris and P. D. Nellist, *Nano Lett.*, 2017, 17, 4003–4012.
- 45 X. J. Zhao, X. L. Xue, Z. X. Guo, Y. Jia, S. F. Li, Z. Zhang and Y. F. Gao, *J. Chem. Phys.*, 2015, 143, 174302.
- 46 G.-F. Wei and Z.-P. Liu, *J. Chem. Theory Comput.*, 2016, **12**, 4698–4706.